

STUDY OF THE 5L-T-TYPE NPC CONVERTER FOR PHOTOVOLTAIC APPLICATION

Tiago L. da Silva, Felipe G. Stein, Joselito A. Heerdt, Yales R. de Novaes

Santa Catarina State University (UDESC), Joinville, Santa Catarina, Brazil

tiagolemes@weg.net, f.g.stein@ieee.org, joselito.heerdt@udesc.br, yales.novaes@udesc.br

Abstract—This work presents the modeling of the control loop for the Five Level (5L) T-Type Neutral-Point Clamped (NPC) converter, for grid-tie photovoltaic application. The control system includes the converter output current control loop and the differential voltage control loop of the input voltage. The results are evaluated by means of a 3kW prototype.

Keywords—5-Level Converter, 5-Level Single Phase Converter, Converter Modeling, Photovoltaic Application

I. INTRODUCTION

The last decades were very important concerning the studies for increasing the efficiency of photovoltaic solar energy generation. A variety of power converters topologies has been studied and, particularly, the non-isolated inverters are capable of having efficiency up to 2% higher when compared against the isolated topologies [1]. However, the non-isolated topologies may cause the circulation of a leakage current [2], [3], due to parasitic capacitance existent between the solar module and its frame, which is grounded together with the metal structure.

Topologies known as the acronyms H5 [4], HERIC [5], FB-DCBP [6] and FB-ZVR [7] are used aiming to reduce or cancel the aforementioned leakage current. With the same objective, the 5L-T-Type NPC with appropriate modulation presents a low leakage current. Furthermore, the application of this topology in full-bridge configuration reduces the input voltage needed to operate at a given grid voltage, which avoids the connection of lots of solar panels in series. Another advantage of the output five levels is the reduction of the output filter requirements or even the increase of the structure power capacity.

Because of the stated reasons, the 5L-T-Type-NPC is an excellent choice for PV application, although there are few publications concerning of its control modeling when applied to grid-tie PV applications. This work presents the modeling of the 5LT-Type-NPC for grid-tie operation.

Firt of all it is presented the modulation technique used, the operating stages and regions. Then the control loops obtained through the modeling of the converter are validated. Finally the controllers calculation is presented and the results obtained.

II. THE TOPOLOGY AND MODULATION

The 5L T-Type NPC topology, shown in the Fig. 1, was first introduced by [8]. The full-bridge configuration of the 5L T-Type NPC allows to apply the total input voltage both in negative and positive output voltage. Such feature is welcome on PV applications, once it reduces the amount

of PV modules panels required to be connected in series, reducing the impact of the shadowing problem [9], when compared to half bridge type topologies.

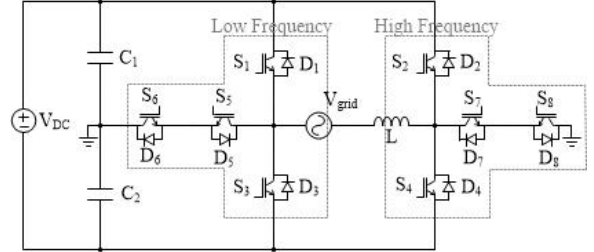


Fig. 1. 5L T-Type NPC topology.

The modulation scheme is hybrid, where one leg of the converter switches at high frequency and the other leg at low frequency, as shown in Fig. 1. The number of commutations is reduced in one leg, which allows the usage of slower switches. For the high frequency leg, one can use faster new generation switches aiming to reduce switching losses and improving the total efficiency of the converter. The modulation scheme uses four carriers in phase, displaced in levels, as shown in Fig. 2. The comparison between the carriers and the modulating function originates the drive signals.

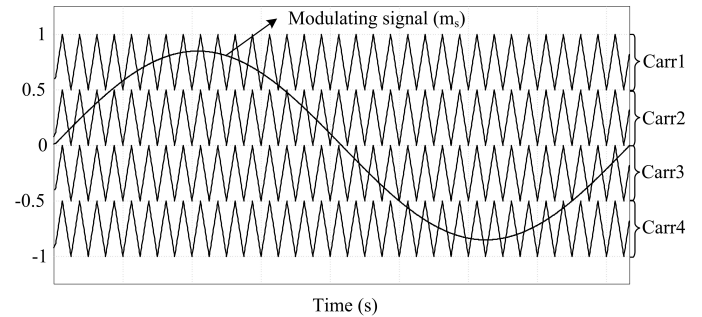


Fig. 2. Carriers distribution and the modulating signal.

The switches S1, S3, S5 and S6 are commutated at low frequency, while S2, S7, S4 and S8 are commutated at high frequency, as shown in Fig. 3. This modulation is based on [8], which addresses the low frequency commutation of the switches aiming to improve the efficiency, while [10] presents free-wheeling paths for the circulation of the current during the dead time intervals, avoiding unwanted stages.

Four operating regions are defined to allow the understanding of the converter operating stages. This operating regions are bounded through the comparison between the modulating signal and the carriers aforementioned. The first operating

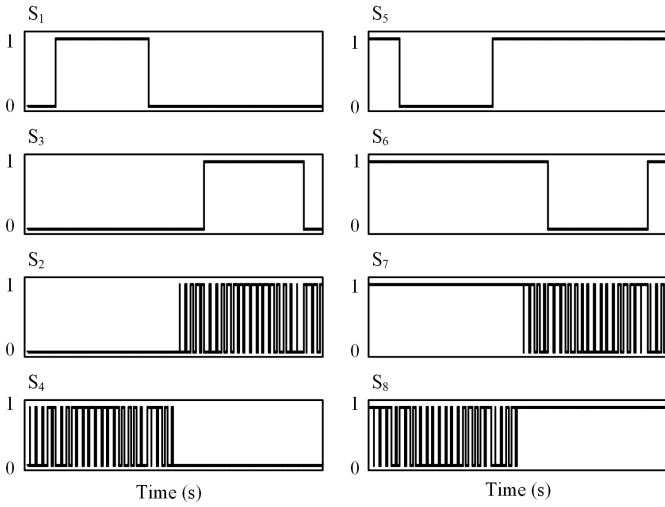


Fig. 3. Gating signals for each switch.

region comprises the comparison of the modulating signal with the second carrier, as shown on Fig. 4. Here the switches S5, S6, and S7 are always gated on. Switches S4 and S8 are applying half of the input voltage to the output at the carrier frequency.

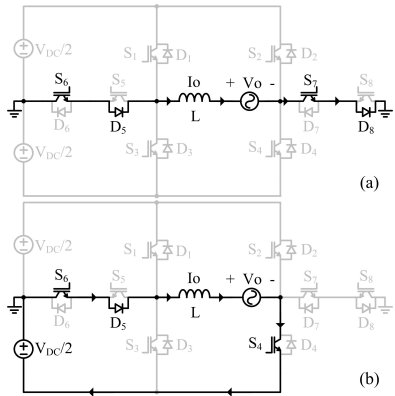


Fig. 4. Operating stages for first region. (a) first stage, (b) second stage.

The second operating region, as shown in Fig. 5, begins when S1 is gated on. It is bounded by the comparison of the carrier number one with the modulating signal. The switches S4 e S8 continue to be commutated at the carrier frequency, operating complementarily. The gated on of switch S1 results in half of the input voltage applied to the output.

The three and four operating regions are deducted similarly.

III. MODELING OF THE CONVERTER

The implemented control structure is presented in Fig. 6. On the diagram there are two control loops that must be modeled: the internal loop, responsible for the control of the output current of the converter, and the external loop, responsible for the control of the differential balancing of the input voltages. Moreover, a PLL algorithm was implemented [11]. The total input voltage depends on the input stage,

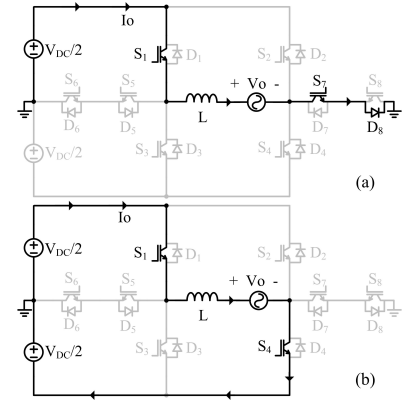


Fig. 5. Operating stages for second region. (a) first stage, (b) second stage.

as it can be composed by a intermediate converter in order to perform the maximum power point tracking operation (MPPT), so this controller is not addressed.

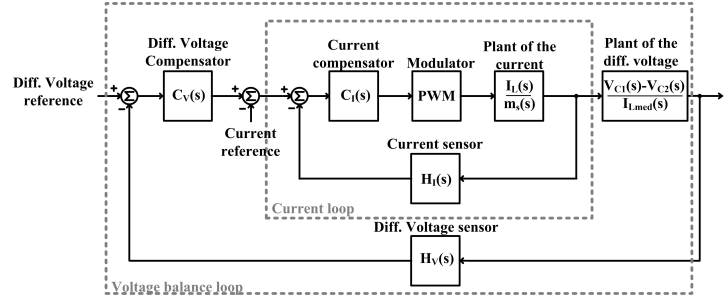


Fig. 6. Block diagram of the implemented control system.

A. Current loop modeling

In order to become possible to inject active power in the distribution grid it is necessary to control the output current, once the output voltage is set by the grid. Taking into account that the pure inductive filter is suitable to achieve the desired output current ripple, an equivalent circuit is obtained to facilitate the analysis and modeling. The circuit is shown in Fig. 7. The inverter is represented as a controlled voltage source, connected to the output filter, represented as an inductor plus resistor. The grid impedance is inductive and resistive as well.

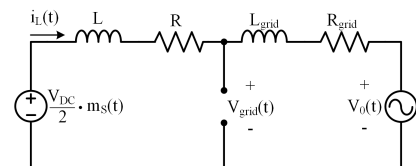


Fig. 7. Equivalent circuit for the modeling of the current plant.

Using the small signals approach, the output current loop is modeled. Applying the Kirchhoff Voltage Law to the circuit of Fig. 7 one obtains (1).

$$L \frac{di_L(t)}{dt} + Ri_L(t) + L_{grid} \frac{di_L(t)}{dt} + R_{grid}i_L(t) = \quad (1)$$

$$V_{dc}m_s(t) - V_0(t)$$

Applying a perturbation $\Delta m_S(t)$ to modulation signal, the output current responds with a perturbation $\Delta i_L(t)$. As showed in (2).

$$\frac{di_L(t)}{dt} + \frac{d\Delta i_L(t)}{dt} (L_f + L_{grid}) + [i_L(t) + \Delta i_L(t)](R + R_{grid}) = \quad (2)$$

$$V_{dc}(m_s(t) + \Delta m_s(t)) - V_0$$

The small signal variation on the input voltage $V_0(t)$ is not considered once the voltage is considered being stable. Applying the Laplace transformation on (2), (3) is obtained. The gain of the current plant is proportional to the input voltage V_{dc} , whereas the frequency of the resulting pole depends on the sum of the converter and the grid impedances.

$$\frac{\Delta i_L(s)}{\Delta m_S(s)} = \frac{V_{dc}}{s(L + L_{grid}) + R + R_{grid}} \quad (3)$$

The Bode diagram is presented in Fig. 8 comparing the simulation (red) and the mathematical model (blue).

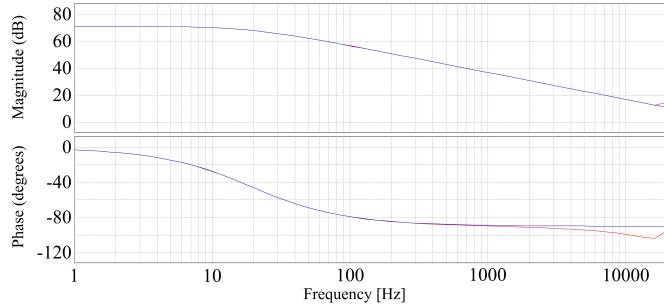


Fig. 8. Model validation for the output current plant.

B. Voltage Balancing loop modeling

For the modeling of the differential voltage balancing loop it is considered the equivalent circuit of the Fig. 9 with a dependent current source for each one of the capacitors.

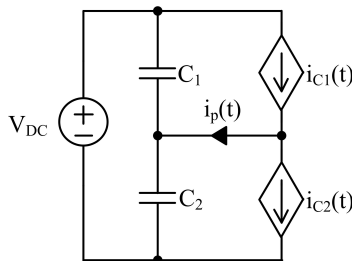


Fig. 9. Equivalent circuit for the modeling of the differential voltage plant.

Equations (4) and (5) represents the behaviour of the neutral point current across time, whereas (6) represents the frequency response using Laplace transformation.

$$i_{C1}(t) - i_{C2}(t) = i_P(t) \quad (4)$$

$$C_1 \frac{dv_{C1}}{dt} - C_2 \frac{dv_{C2}}{dt} = i_P(t) \quad (5)$$

$$V_{C1}(s) - V_{C2}(s) = \frac{I_P(s)}{sC_1} \quad (6)$$

Where $V_{C1}(s)$ e $V_{C2}(s)$ are the voltages of the capacitors C_1 and C_2 respectively and $I_P(s)$ represents the current at the neutral point of the capacitors. The neutral point current $i_p(t)$ is related to the output current and this relationship is constant and is obtained as the constant K_{dif} in (7).

$$I_P(s) = K_{dif} I_L(s) \quad (7)$$

First the medium value of I_p within one grid cycle is obtained in (8).

$$I_P = \frac{2}{2\pi} \left[\int_{\theta_0}^{\theta_1} i_P^{R1} d\theta + \int_{\theta_1}^{\theta_2} i_P^{R2} d\theta + \int_{\theta_2}^{\theta_3} i_P^{R1} d\theta \right] \quad (8)$$

Where $\langle i_P \rangle^{R1}$ and $\langle i_P \rangle^{R2}$ are the instantaneous medium values of the currents in the first and second region, respectively. Also θ_0 and θ_1 represents the limits of the first region, θ_1 and θ_2 the second region and θ_2 and θ_3 the third region.

Evaluating the operating stages of the converter it is possible to obtain the medium value of the neutral current, being the contribution of the first region of operation given by (9):

$$i_P^{R1} = \frac{1}{T_S} \int_{t_0}^{t_0 + d_4^{R1} T_s} I_L(\theta) dt = I_L(\theta) d_4^{R1}(\theta) \quad (9)$$

The contribution of the second region of operation is given by (10):

$$i_P^{R2} = \frac{1}{T_S} \int_{t_0 + d_4^{R1} T_s}^{t_0 + T_s} -I_L(\theta) dt = I_L(\theta) (d_4^{R1}(\theta) - 1) \quad (10)$$

Where T_s is the switching period, $d_4^{R1}(\theta)$ and $d_4^{R2}(\theta)$ the duty cycle of $S4$ on the operating regions one and two, respectively, shown in (11), (12) and (13).

$$d_4^{R1}(\theta) = 2m_s(\theta) \quad (11)$$

$$d_4^{R2}(\theta) = 2m_s(\theta) - 1 \quad (12)$$

$$m_s(\theta) = m_a \sin(\theta) \quad (13)$$

Where m_a is the amplitude modulation index. Finally it is possible to obtain the value of K_{dif} , shown in (14).

$$K_{dif} = \frac{2[2m_a - \pi + 2\arcsin(\frac{1}{2m_a})]}{\pi} \quad (14)$$

Once the relation between $I_L(s)$ and $I_P(s)$ is known it is necessary to obtain the relationship between the difference of the capacitors voltages and $I_L(s)$. This is showed in the (15).

$$\frac{V_{C1}(s) - V_{C2}(s)}{I_L(s)} = \frac{2[2m_a - \pi + 2\arcsin(\frac{1}{2m_a})]}{(sC_1\pi)} \quad (15)$$

In order to obtain a validation of the model, the step response is evaluated. Fig. 10 shows the converter response (red) and the mathematical model (blue).

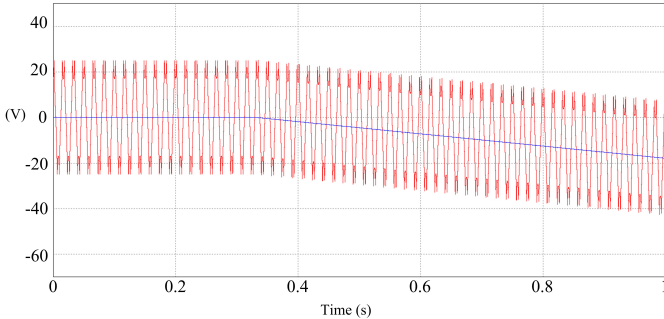


Fig. 10. Model validation for the capacitor differential voltage.

IV. CONTROLLERS DESIGN

A prototype of 3 kW was built considering a grid voltage of 220V and an input voltage of 360V_{dc}. Using a commutation frequency of 40 kHz, a 10% ripple of the output current with a pure inductive filter of 900 μ H is obtained. The value of the individual input capacitors is 820 μ F. Equations (16) and (17) show the open loop transfer functions for the current loop and the differential voltage loop in the w-plane, respectively. With the Tustin approximation it was obtained a digital representation of the control plants. Finally the models were designed using the complex w-plane. The control platform utilized a DSP.

$$\frac{\Delta I_L(w)}{\Delta m_s(w)} = \frac{-0.11417(w + 129.710^3)(w - 80.0410^3)}{(w + 79.0210^3)(w + 111.1)} \quad (16)$$

$$\frac{V_{C1}(w) - V_{C2}(w)}{I_L(w)} = \frac{-0.008(w - 1.210^3)}{w} \quad (17)$$

The output current controller is a resonant controller [12], featured by having two resonant poles in 60Hz with damping of 0.1×10^{-6} and two complex zeros located in a frequency slightly higher than 60Hz, with damping of 0.7, located with the objective of correcting the phase margin of the system, as can be seen in Fig. 11. The equation (18) shows the transfer function of the resonant controller used, on the z-plane.

$$C_i(Z) = \frac{1.041z^3 - 0.9949z^2 - 1.04z + 0.9959}{z^3 - 1.778z^2 + 0.5564z + 0.2218} \quad (18)$$

The choice of the controller for the differential balancing is based upon the need to improve the phase margin of the system. The controller is a leading phase, thereby, the frequencies of the pole and the zero are chosen to obtain phase margin bigger than 50 degrees. The Fig. 12 shows the Bode diagram of the open loop transfer function without the controller $G_{ma,nc}(w)$, with the controller $C(w)$ and only the controller $C(w)$ all in the w-plane. The equation (19) shows the transfer function of the controller used, in the z-plane.

$$C_V(Z) = \frac{1.910^{-3}z^2 + 2.710^{-6}z + 1.910^{-3}}{z^2 + 1.985z + 0.9853} \quad (19)$$

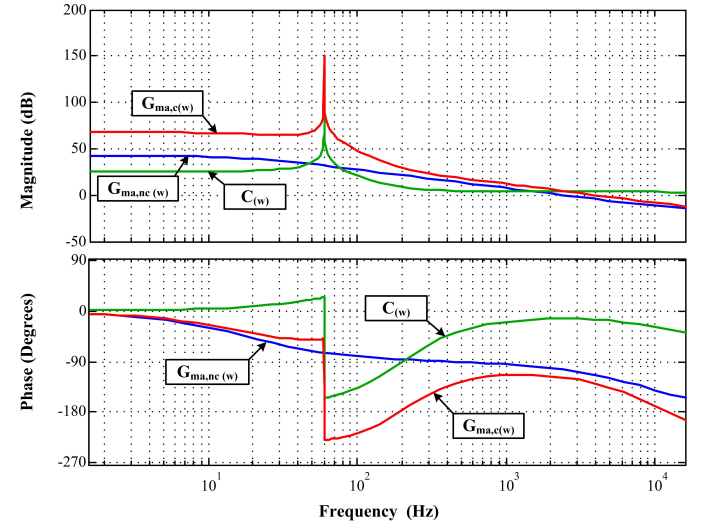


Fig. 11. Open loop Bode diagram of the overall system $G_{ma,nc}(w)$, for the used controller $C(w)$ and for the controlled system $G_{ma,c}(w)$ for the current control.

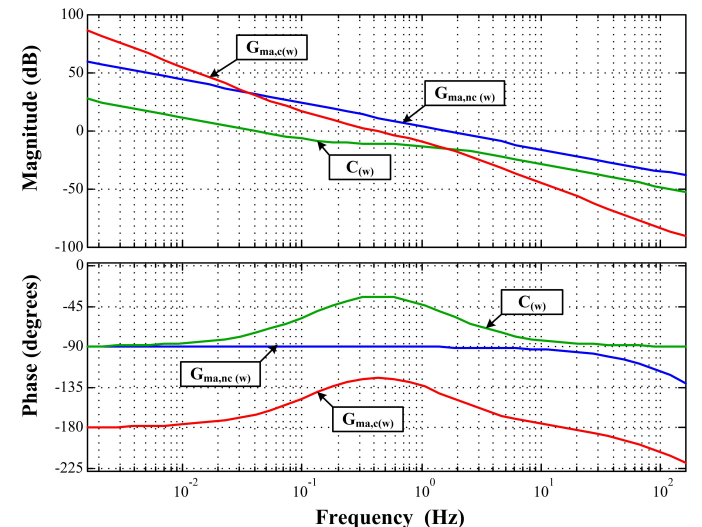


Fig. 12. Open loop Bode diagram of the overall system $G_{ma,nc}(w)$, for the used controller $C(w)$ and for the controlled system $G_{ma,c}(w)$ for the differential voltage balancing.

V. EXPERIMENTAL RESULTS

The main objective of the results here presented is the validation of the control loops. Fig. 13 presents the grid voltage and the output current. It is possible to validate the non-perturbed behavior of the control at nominal power, once the RMS value of the output current is 13.1A. Considering the grid voltage of 220V, the power injected to the grid is 2882W. The mean value of the output current is also very important, because it might does not pass 0.5% of the nominal current, according to distribution transformer standards. The obtained result is 77mA which represents 0.4% of the nominal current. Moreover with Fig. 13 was possible to calculate the THD of current, what resulted in 6% of harmonic distortion. The dynamic of the current controller is validated with load step at the amplitude of the current reference and the result showed in Fig. 14, where the current changes from 10A peak to 12A peak in a few cycles of the grid frequency.

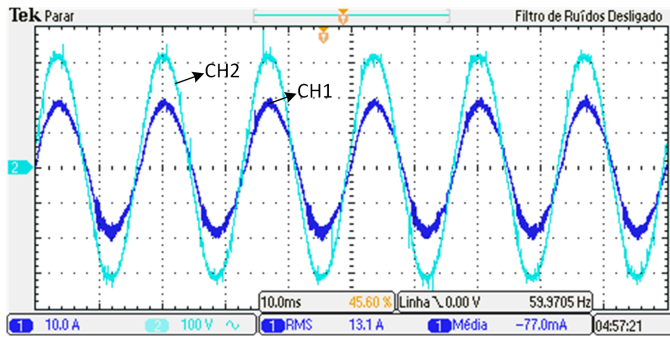


Fig. 13. Output current (CH1, 10A/div), grid voltage (CH2, 100V/div).

The third result obtained is intended to validate the behavior of the differential voltage balancing loop. With the system operating in steady state it was applied a step with a mean value directly on the reference of the current loop (blue), being possible to observe a ripple in the difference of the voltage on each capacitor (in green at C1 and in violet at C2) and approximately 2.2 seconds after the controller completely restored the balance.

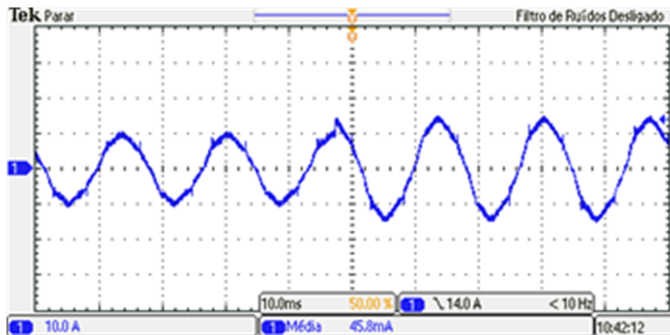


Fig. 14. Output current (CH1, 10A/div).

VI. CONCLUSION

Through the results obtained it is possible to evaluate the converter at nominal power with static operation and with

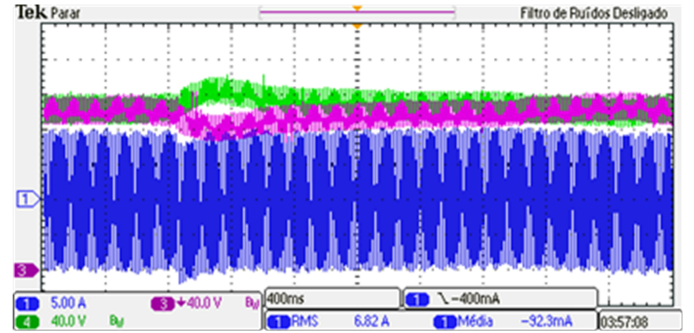


Fig. 15. Dynamic Evaluation for the differential voltage control. (CH1, 10A/div), (CH3, 40V/div), (CH4, 40V/div)

a step response at the current. It is validated the modeling of the current loop and its resonant controller design. The dynamic of the input capacitors differential voltage loop is evaluated, applying a step at the mean value on the reference of the output current controller, specially showing the validity of the differential voltage loop model and the design of its controller. As a future work, the study of the impact that the variation of the modulation index causes on the differential voltage control loop, once that for photovoltaic applications the modulation index varies along the operation during the day. Furthermore, the improvement on the resonant controller with resonant peaks on the frequencies of 3, 5 and 7 times the nominal grid frequency would reduce the THD of the output current.

ACKNOWLEDGEMENT

The authors would like to thank support of FITEJ Foundation and FAPESC foundations during the work.

REFERENCES

- [1] R. Teodorescu, M. Liserre, and P. Rodriguez. *Converters for Photovoltaic and Wind Power Systems*. John Wiley and Sons, 2011.
- [2] Eugenio Guba, Pablo Sanchis, Alfredo Ursa, Jess Lpez, and Luis Marroyo. Ground currents in single-phase transformerless photovoltaic systems. *PROGRESS IN PHOTOVOLTAICS: RESEARCH AND APPLICATIONS*, 15:629650, 2007.
- [3] G. Spagnuolo, G. Petrone, S.V. Araujo, C. Cecati, E. Friis-Madsen, E. Gubia, D. Hissel, M. Jasinski, W. Knapp, M. Liserre, P. Rodriguez, R. Teodorescu, and P. Zacharias. Renewable energy operation and conversion schemes: A summary of discussions during the seminar on renewable energy systems. *Industrial Electronics Magazine, IEEE*, 4(1):38–51, March 2010.
- [4] Matthias Victor, Frank Greizer, Sven Bremicker, and Uwe Hbler. Method of converting a direct current voltage from a source of direct current voltage, more specifically from a photovoltaic source of direct current voltage, into a alternating current voltage, 2008.
- [5] Herbert Schmidt, Christoph Siedle, and Jrgen Ketterer. Dc/ac converter to convert direct electric voltage into alternating voltage or into alternating current, 2006.

- [6] Calahorra Javier Coloma, Senosiain Roberto Gonzalez, Taberna Jesus Lopez, Palomo Luis Marroyo, and Gurpide Pablo Sanchis. Single-phase inverter circuit for conditioning and converting dc electrical energy into ac electrical energy, 2009.
- [7] T. Kerekes, R. Teodorescu, P. Rodriguez, G. Vazquez, and E. Aldabas. A new high-efficiency single-phase transformerless pv inverter topology. *Industrial Electronics, IEEE Transactions on*, 58(1):184–191, Jan 2011.
- [8] Antonio Coccia, Francisco Canales, Leonardo-Augusto Serpa, and Mikko Paakkinnen. Five-level inverter, 2010.
- [9] Qing shan Xu, Loi Lei Lai, Norman Tse, and K. Ichiyanagi. Hybrid behaviors analysis of photovoltaic array performance. In *Machine Learning and Cybernetics, 2009 International Conference on*, volume 6, pages 3448–3456, July 2009.
- [10] J.A. Heerdt, S.A. Mussa, and M.L. Heldwein. Semiconductors current efforts and losses evaluation for single-phase three-level regenerative pwm rectifiers. In *Industrial Electronics (ISIE), 2010 IEEE International Symposium on*, pages 1046–1051, July 2010.
- [11] Fernando P. Marafo, Sigmar M. Deckmann, Jos A. Pomilio, and Ricardo Q. Machado. Metodologia de projeto e anlise de algoritmos de sincronismo. *SOBRAEP*, 2005.
- [12] J.R. Gazoli, M.E. de Oliveira F, M.F. Espindola, T.G. de Siqueira, M.G. Villalva, and E. Ruppert. Resonant (p+res) controller applied to voltage source inverter with minimum dc link capacitor. In *Power Electronics Conference (COBEP), 2011 Brazilian*, 2011.